Realization of Topological Phase in a Chiral Honeycomb Lattice Model

Genki Yonezawa,[1,*] Jun-ichi Fukuda,[1,2] and Toshikaze Kariyado[3]

[1]*Department of physics, Faculty of Science, Kyushu University, Fukuoka, Japan*

[2]*International Institute for Sustainability with Knotted Chiral Meta Matter (WPI-SKCM²), Hiroshima University 1-3-1 Kagamiyama, Higashi-Hiroshima, Hiroshima 739-8526, Japan*

[3]*Reserch Center for Materials Nanoarchitectonics(MANA), National Institute for Materials Science, Tsukuba, Japan*

Abstract

We investigate topological properties of a chiral honeycomb lattice model with next-nearest-neighbor hoppings characterized by the reflection symmetry breaking. Topological nontriviality is detected by analyzing effective Dirac Hamiltonian, and confirmed by numerical and analytical study of the emergence of topological edge states at the boundaries between topologically distinct regions. We have also discovered that a novel asymmetric edge current attributable to chirality can be excited without any involved phase shifts in input sources to pick up one of the pseudospin components.

I. Introduction

Band theory, which specifies band energies and wave functions by momentum in Brillouin zone, has been traditionally used in solid state physics. Historically, band gaps or effective masses, which are encoded in band energies, play important roles in relation to the semiconductor technology. The study of quantum Hall effect (QHE) [1, 2] then brought a new approach to classification of band structures, namely the use of topological invariants like Chern numbers that are encoded in the connection of the wave functions in the Brillouin zone. Although the QHE requires the time-reversal symmetry breaking, it has been recognized that various systems with time-reversal symmetry can also exhibit topological phases, realized by spin-orbit coupling [3–5], crystalline symmetry [6], and so on.

As an ideal platform for investigating topological phases, tight-binding models on honeycomb lattice have been attracting interest as a system exhibiting the Dirac band structure. One of the most interesting model was proposed by Haldane [7], and a quantum anomalous Hall effect (QAHE) can be realized by introducing next-nearest-neighbor (NNN) hopping with complex value. These complex hoppings can also be induced by considering the intrinsic spin-orbit coupling (SOC) in the honeycomb lattice, and spinful electron systems show a quantum spin Hall effect (QSHE) [8–10]. After

* g.yonezawa@cmt.phys.kyushu-u.ac.jp

these theoretical predictions of QAHE and QSHE, many studies have been established to realize topological phases on the honeycomb lattice [11–18]. QAHE has also been explored to support topological states in metamaterial settings, such as Floquet systems [19–21] or photonic crystals [22, 23].

As another direction of study, a modulated honeycomb lattice model proposed by Wu and Hu [24] should be mentioned as a system exhibiting a quantum psuedospin Hall effect (QpSHE). They take a hexagonal unit cell and treat the honeycomb lattice as a triangle network of hexagons. By tuning the ratio of intra-hexagon hopping to inter-hexagon hopping, a topological phase transition can be realized, accompanied by a band inversion at Γ point. This model has wide application to metamaterials, because it does not require SOC. In fact, their setup is also applicable to a photonic crystal made of only a dielectric medium [25, 26].

In the studies of honeycomb lattice models, the sublattice symmetry often plays an important role. Only with the nearest-neighbor (NN) hoppings (which is supposed to give a minimal model for graphene), a honeycomb lattice model has the sublattice symmetry. The sublattice symmetry is also preserved in the case of QpSHE in the honeycomb lattice when there is no NNN hoppings. In contrast, the honeycomb models for QAHE and QSHE breaks the sublattice symmetry due to the complex NNN hoppings [27, 28].

Although NNN hopping on honeycomb lattice brings exotic phenomena, the previous study of the QpSHE did not focus on how the sublattice symmetry breaking affects the topological phase transition. Moreover, the effect of chirality characterized by the reflection symmetry breaking has not been explored.

The aim of the present study is to investigate how chirality affects the classification of the band topology and the edge transport characteristic of the non-trivial band topology. We focus on the cases in which time reversal symmetry is preserved. As mentioned above, a tight-binding model with the honeycomb structure has been regarded as an ideal platform for topological phases, and here we propose a chiral honeycomb lattice model by extending the model proposed by Wu and Hu [24] and introducing chirality in the NNN hopping. The setup of our model also breaks the above-mentioned sublattice

symmetry, which complements the previous studies of the QpSHE.

The rest of this paper is organized as follows. In Sec.II, we start with describing the setup of our tight-binding model. As we will discuss in detail there, our model is applicable not only to quantum fermionic system but also a classical system characterized by a dynamical matrix instead of a quantum Hamiltonian. Then in Sec.III, we conduct topological classification by using effective Hamiltonian, and calculate energy dispersions. The validity of analytically shown topological classification is numerically confirmed by calculating interface states. In Sec.V, we calculate interface transport to elucidate the effect of chirality. We conclude this paper and make discussions in Sec.VI.

II. Model

In order to consider how chirality affects the behavior of a topologically non-trivial system, we specifically discuss a two-dimensional fermionic system or its corresponding classical harmonic oscillator system. Generally, band structures is not only for quantum systems but also for classical systems, such as frequency spectra of dynamical matrices in a spring-mass model [29]. Therefore, topological nontriviality of band structures could be detected by using both fermionic system and harmonic oscillator system.

We first consider a two-dimensional tight-binding model on a honeycomb lattice with NN and NNN hoppings. Figure 1 presents the schematic illustration of the model and the geometry. Due to the modulation in hoppings, the primitive unit cell is a hexagon containing six sites instead of two in the pristine honeycomb lattice model. Then, the unit vectors for the modulated honeycomb lattice are $\boldsymbol{a}_1 = (3a_0/2, \sqrt{3}a_0/2)^T$ and $\boldsymbol{a}_2 = (-3a_0/2, \sqrt{3}a_0/2)^T$, where a_0 is a lattice constant for the pristine case. The Hamiltonian reads

$$H = \sum_{\langle i,j \rangle} t_{ij} c_i^\dagger c_j + \sum_{\langle\langle i',j' \rangle\rangle} t_{i'j'} c_{i'}^\dagger c_{j'}. \tag{1}$$

Here c_i ($c_i^\dagger$) is the annihilation (creation) operator for electrons. $\langle i,j \rangle$ denotes nearest neighbors, and $\langle\langle i',j' \rangle\rangle$ denotes next nearest neighbors. As NN hoppings, we consider both intrahexagon hopping t_0 and interhexagon hopping t_1, as depicted in FIG. 1. On

the other hand, as NNN hoppings, we only consider interhexagon hopping. Furthermore, we classify the interhexagon hoppings into two types, and respectively assign t_2 and t_3 to introduce chirality on the system. The two types of hoppings are illustrated in FIG. 1.

The reflection symmetry breaking can be introduced by setting t_2 unequal to t_3. Indeed, as depicted in FIG. 2, the t_2 bonds are the mirror image of the t_3 bonds, where the reflection plane is on the vertical line. This means that the system becomes chiral when $t_2 \neq t_3$, because the roles of t_2 and t_3 are swapped before and after the reflection operation.

As mentioned above, this model is an extension of the model proposed by Wu and Hu [24], who considered a quantum psuedospin Hall effect on a modulated honeycomb lattice. Their setup is also applicable to a photonic crystal made of only a dielectric medium [25], which yields a venue for experimental validations [26].

In the following, we limit ourselves to the case with the real-valued hopping t_0, t_1, t_2, t_3, unlike Haldane model. This makes it straightforward to realize the model in any artificial systems like photonic crystals. Without complex-valued hoppings, the time-reversal symmetry is preserved in our setup. We emphasize that we handle the case of $t_2 \neq t_3$, in which the system becomes chiral.

In principle, the Hamiltonian Eq. (1) can be mapped to a dynamical matrix Γ of a classical system. Here we specifically consider a mass-spring system in which potential energy can be written as

$$V\{\boldsymbol{x}\} = \frac{1}{2}\sum_i \sum_{j>i} k_{ij}(x_i - s_{ij}x_j)^2 + \frac{1}{2}\sum_i \epsilon_i x_i^2, \tag{2}$$

as a function of dynamical variables $\boldsymbol{x}$. The number of components in $\boldsymbol{x}$ corresponds to the number of degrees of freedom in a given system. The first term represents couplings between different degrees of freedom, with spring constants $k_{ij} > 0$ and s_{ij} being $+1$ or -1. The way to choose ± 1 for s_{ij}s in a spring-mass model is explained in FIG. 3. When a spring stores elastic energy for anti-phase motion of two connected mass points, $s_{ij} = 1$ for this spring, while when it stores elastic energy for in-phase motion of two connected mass points, $s_{ij} = -1$ for this spring. The second term, introduced for

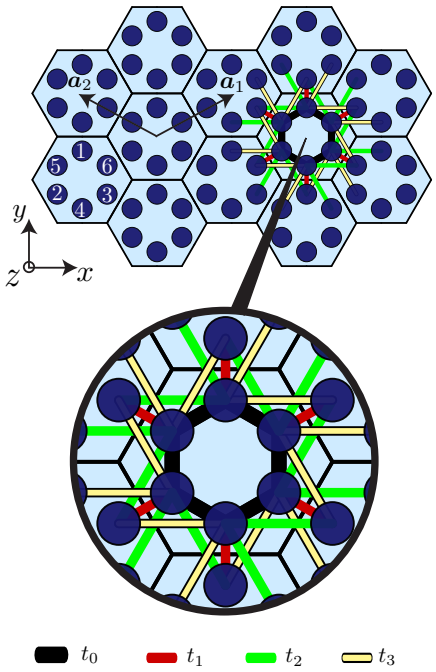

FIG. 1. (color online) Schematic illustration of the tight-binding model treated in this article. The NN hoppings inside unit cells are denoted by t_0 (black solid lines), and the NN hoppings between unit cells are denoted by t_1 (red solid lines). The NNN hoppings are also introduced as t_2 (green solid lines) and t_3 (yellow solid lines).

later convenience, is a local term that, in a spring-mass model, can be understood as a connection between the mass and the ground. Here ϵ_i is positive. The dynamical matrix of the system is given by

$$\Gamma_{ij} = \frac{\partial^2 V}{\partial x_i \partial x_j} = \left(\epsilon_i + \sum_l k_{il} \right) \delta_{ij} - s_{ij} k_{ij}. \tag{3}$$

By appropriately choosing ϵ_is, k_{ij}s and s_{ij}s such that $\epsilon_i + \sum_l k_{il}$ is equal to a constant ϵ independent of i, and that $s_{ij}k_{ij}$, which can be positive or negative, is equal to the hopping energies of the quantum counter part, the dynamical matrix Γ can be written as

$$\Gamma_{ij} = \epsilon \delta_{ij} - h_{ij}, \tag{4}$$

where h_{ij} is hopping energies in the Hamiltonian. By setting ϵ to be sufficiently large, Γ

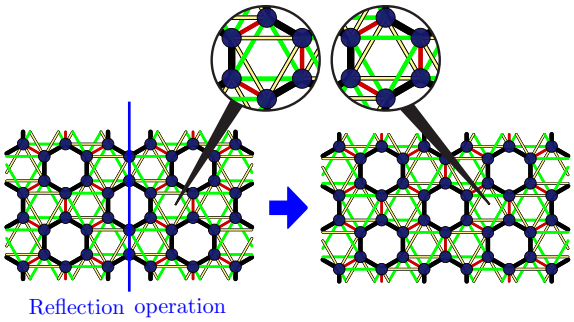

FIG. 2. (color online) The system after the reflection operation. Due to the existence of NNN hoppings t_2 and t_3 the reflected system can not be superposed onto the original one.

can be positive definite. Thus, one can construct a classical system where its dynamical matrix Γ is equal to H (with a constant shift of ϵ).

After establishing the mapping of Eq. (4), the band structure of the Hamiltonian (1) has two interpretations: the energy spectra in the quantum system and the spectra of the square of the frequency (modified by the constant shift ϵ) in the classical system. For convenience, we investigate the topological properties (Sec. III and IV) by using the Hamiltonian H, whereas we discuss the interface transport on a classical ribbon structure with the dynamical matrix Γ (Sec. V), since the coupling with external forces can be understood more intuitively in classical systems.

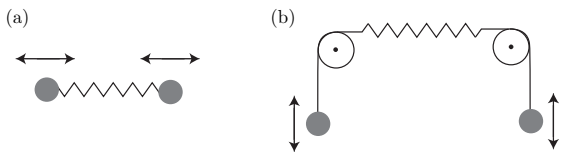

FIG. 3. (color online) The physical meaning of s_{ij} in a spring-mass model. (a)$s_{ij} = +1$. The masses are connected by a spring directly, then the spring acquires elastic energy for *anti*-phase oscillation. (b)$s_{ij} = -1$. The pulleys change the coordinate axes, and s_{ij} is now negative. In this case the spring acquires elastic energy for *in*-phase oscillation.

III. Band structures and effective Hamiltonian

To elucidate the topological properties of our chiral model given by Hamiltonian Eq. (1), we calculate its energy dispersions. We first consider the case where the system is periodic with respect to $\boldsymbol{a}_1$, $\boldsymbol{a}_2$. By Fourier transforming Eq. (1), the Hamiltonian as a function of momentum $\boldsymbol{k}$ is written as

$$
\begin{aligned}
H(\boldsymbol{k}) &= \begin{pmatrix} F(\boldsymbol{k}) & D(\boldsymbol{k}) \\ D(\boldsymbol{k})^\dagger & F(\boldsymbol{k})^T \end{pmatrix}, \\
D(\boldsymbol{k}) &= \begin{pmatrix} t_1 e_1^*(\boldsymbol{k}) e_2^*(\boldsymbol{k}) & t_0 & t_0 \\ t_0 & t_1 e_1(\boldsymbol{k}) & t_0 \\ t_0 & t_0 & t_1 e_2(\boldsymbol{k}) \end{pmatrix}, \\
F(\boldsymbol{k}) &= \begin{pmatrix} 0 & t_2 e_1^*(\boldsymbol{k}) + t_3 e_1^*(\boldsymbol{k}) e_2^*(\boldsymbol{k}) & t_2 e_1^*(\boldsymbol{k}) e_2^*(\boldsymbol{k}) + t_3 e_2^*(\boldsymbol{k}) \\ t_2 e_1(\boldsymbol{k}) + t_3 e_1(\boldsymbol{k}) e_2(\boldsymbol{k}) & 0 & t_2 e_2^*(\boldsymbol{k}) + t_3 e_1(\boldsymbol{k}) \\ t_2 e_1(\boldsymbol{k}) e_2(\boldsymbol{k}) + t_3 e_2(\boldsymbol{k}) & t_2 e_2(\boldsymbol{k}) + t_3 e_1^*(\boldsymbol{k}) & 0 \end{pmatrix},
\end{aligned}
\tag{5}
$$

where $e_l(\boldsymbol{k}) = e^{i\boldsymbol{k}\cdot\boldsymbol{a}_l}$ $(l = 1, 2)$.

Figure 4 shows plots of the energy dispersion for the Hamiltonian Eq. (5) by setting the hopping energies t_0, t_1, t_2, t_3 to several typical values. Importantly, a band inversion occurs by changing the value of t_1 appropriately. This can be confirmed by plotting the values of $|\langle u_{\boldsymbol{k}}^n | d_+ \rangle|$ as line colors, where $|u_{\boldsymbol{k}}^n\rangle$ is the periodic part of Bloch function labeled by index n and Bloch wave vector $\boldsymbol{k}$. We see that the colors of the band edges near $E = 0$ at the Γ-point are exchanged between Figs. 4(a) and 4(c). For the system with $t_1 = t_0$ [Fig. 4(b)], double Dirac cones appear at $E = 0$.

In the low energy region around the Γ point, the effective Hamiltonian can be derived as

$$
\mathcal{H}^{(\mathrm{eff})}(k_x, k_y) \simeq \begin{pmatrix} H_+(k_x, k_y) & 0 \\ 0 & H_-(k_x, k_y) \end{pmatrix}, \tag{6}
$$

where

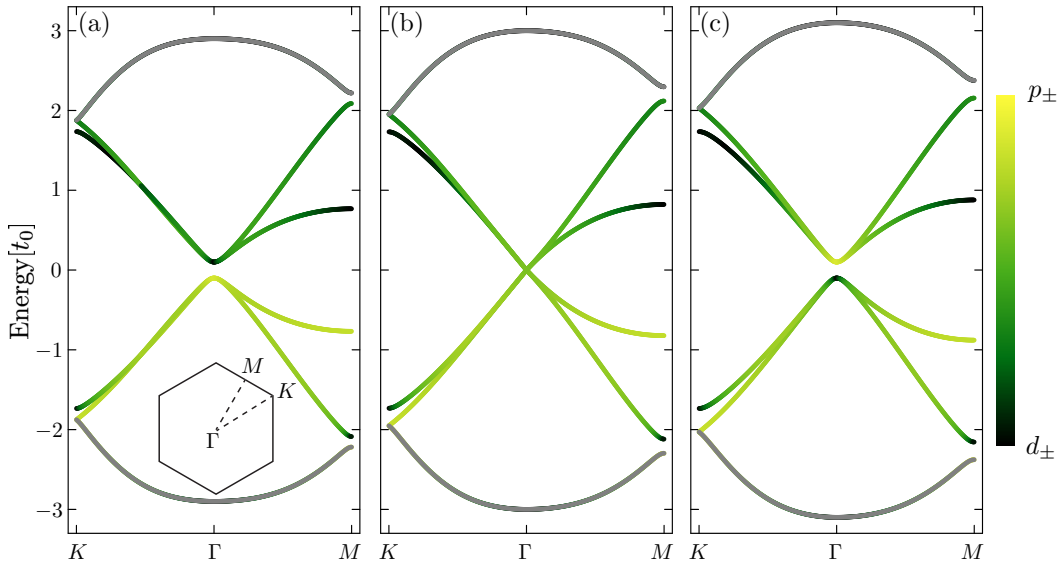

FIG. 4. (color online) Energy dispersions for the system given by Eq.(1). In all panels, we set $t_2 = 0.3t_0$ and $t_3 = -0.3t_0$: (a) $t_1 = 0.9t_0$, (b) $t_1 = t_0$, (c) $t_1 = 1.1t_0$. The color maps are for the values of $|\langle u^n_{\boldsymbol{k}}|d_+\rangle|$. $|p_\pm\rangle$ and $|d_\pm\rangle$ are pseudo-spin modes, and their definitions are given in Appendix A.

$$H_\pm(k_x, k_y) = -(t_2 + t_3)I + (t_0 - t_1)\sigma_z + \frac{t_1|\boldsymbol{a}_1|}{2}(\pm k_x\sigma_x + k_y\sigma_y). \tag{7}$$

The derivation is given in Appendix A. This Dirac Hamiltonian Eq. (7) clarifies the origin of the band inversion in FIG. 4, where the band inversion is induced by varing the hopping energy t_1. In the context of the Dirac Hamiltonian, the sign of the Dirac mass $m := t_0 - t_1$ can be flipped by changing t_1, which explains the origin of the gap and infers that the two states in Figs. 4(a) and 4(c) are topologically distinct with each other.

For simplicity, we focus on the sign of the mass term m to pick up topological characters of the system, namely we say two states with the opposite signs of m topologically distinct. Strictly speaking, a topological index often requires information of global structure of Bloch wave functions in the entire Brillouin zone (as the Chern number), not only information of the band order at a single momentum (Γ-point in this case).

However, a description by a Dirac equation with spatial modulation in its mass term gives a universal understanding of topologically protected edge/interface states. This will be confirmed in the following analysis.

We note that a complementary view can be given by further analysis using $C_2\mathcal{T}$ symmetry. It has been shown that in crystals with $C_2\mathcal{T}$ symmetry, the Wilson loop spectra can be utilized to define a $\mathbb{Z}_2$ index [30]. While next-nearest-neighbor hopping terms break sublattice symmetry in our model, $C_2\mathcal{T}$ symmetry remains intact. Therefore, rigorous $\mathbb{Z}_2$ classification can still be applied. We have included a discussion on Wilson loops in Appendix B.

IV. Topological edge state

In this section, we analyze localized states at the boundary between two regions with distinct topology. We begin with the analytical approach using the low-energy effective Dirac theory. Let us consider a case where the periodic boundary condition is imposed only in the x direction. There is a boundary normal to the y direction where the sign of the mass term switches: $t_0 - t_1 = m_0 > 0$ for $y > 0$ and $t_0 - t_1 = -m_0$ for $y < 0$. In the x direction, k_x is a good quantum number because of the existence of the periodic boundary condition. In the y direction, however, we apply a continuous approximation by replacing k_y with $-i\partial_y$ to take into account the spatial dependence of m. The eigenvalue equation of $H_+(k_x, k_y)$ then becomes

$$\begin{pmatrix} -(t_2+t_3) + m_0\mathrm{sgn}(y) & v(k_x - \partial_y) \\ v(k_x + \partial_y) & -(t_2+t_3) - m_0\mathrm{sgn}(y) \end{pmatrix} \begin{pmatrix} \phi_1 \\ \phi_2 \end{pmatrix} = E \begin{pmatrix} \phi_1 \\ \phi_2 \end{pmatrix}, \tag{8}$$

where $v := t_1|\boldsymbol{a}_1|/2$. Rewriting this equation in a new basis $\phi_\pm = \phi_1 \pm \phi_2$, the eigenvalue equation yields

$$\begin{pmatrix} -(t_2+t_3) + vk_x & m_0\mathrm{sgn}(y) + v\partial_y \\ m_0\mathrm{sgn}(y) - v\partial_y & -(t_2+t_3) - vk_x \end{pmatrix} \begin{pmatrix} \phi_+ \\ \phi_- \end{pmatrix} = E \begin{pmatrix} \phi_+ \\ \phi_- \end{pmatrix}. \tag{9}$$

When $m_0/v > 0$, the solution obtained under the conditions that the wavefunction converges at $y = \pm\infty$ and is continuous at $y = 0$ is

$$E_+ = -(t_2 + t_3) - vk_x, \begin{pmatrix} \phi_+ \\ \phi_- \end{pmatrix} \propto \begin{pmatrix} 0 \\ \exp(-(m_0/v)|y|) \end{pmatrix}. \tag{10}$$

The eigenvalue equation for H_- is obtained by simply replacing k_x of Eq.(9) by $-k_x$. The eigenenergy and states become

$$E_- = -(t_2 + t_3) + vk_x, \begin{pmatrix} \phi_+ \\ \phi_- \end{pmatrix} \propto \begin{pmatrix} 0 \\ \exp(-(m_0/v)|y|) \end{pmatrix}. \tag{11}$$

Thus, by solving the eigenvalue equations of $\mathcal{H}^{(\mathrm{eff})}$, one obtain the solutions such that the eigenenergies $E_\pm$ intersect linearly at $E_0 := -(t_2 + t_3)$. In addition, the corresponding eigenstates are exponentially localized at the boundary $y = 0$. These localized states are protected by the difference of topology, i.e. the difference of the sign of mass term in Eq. (A15), which confirms the usefulness of the mass-term based topological classificaiton.

Next, we move on to the numerical approach using the tight-binding model. In order to discuss boundary states, we consider a system where a region of $t_1 = 1.1t_0$ is sandwiched between two regions of $t_1 = 0.9t_0$ as shown in FIG. 5(a). Note that $\boldsymbol{a}_1$ direction is horizontal in FIG. 5(a). Then, periodic boundary conditions are imposed on $\boldsymbol{a}_1$ and $\boldsymbol{a}_2$ directions, respectively. With this construction of the interface, $\boldsymbol{a}_2$ remains to be a unit vector, i.e., there is no superstructure in $\boldsymbol{a}_2$ direction, and we can calculate energy dispersion as a function of the momentum along the interface $k_\parallel$. The calculated dispersion is in FIG. 5(b), showing new states in the bulk gap that intersect linearly at $k_\parallel = 0$, which is consistent with the analytical discussions above. Plotting the square norm of the corresponding wave function (FIG. 5(c)) also shows that it is localized at the boundaries.

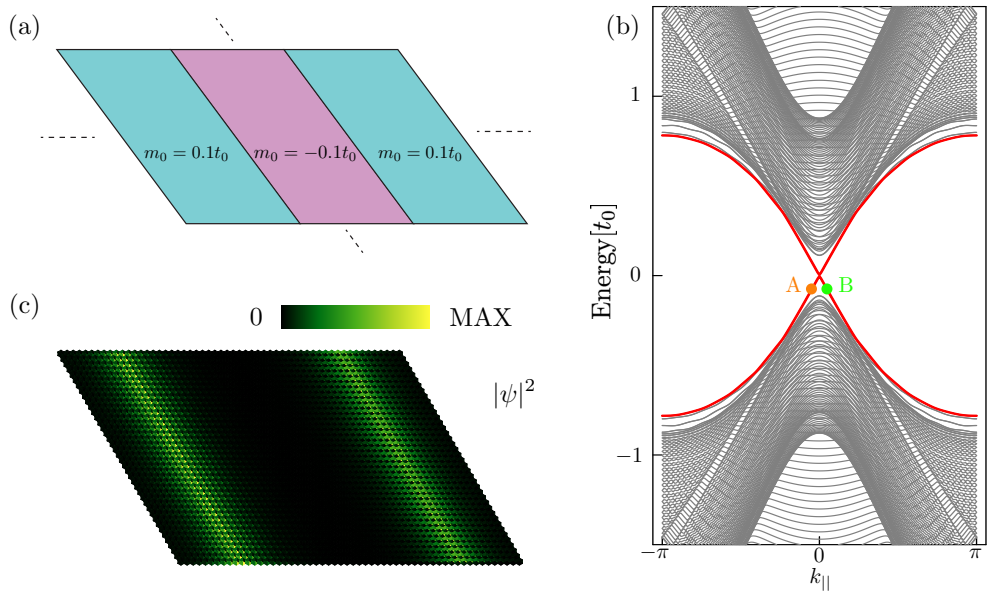

FIG. 5. (color online) The hopping enegies of chirality are set to $t_2 = 0.3t_0$ and $t_3 = -0.3t_0$. (a) Schematic illustration of the system being simulated, with a region of $t_1 = 1.1t_0$ bounded by two regions of $t_1 = 0.9t_0$. (b) energy dispersions (c) The square of wave functions corresponding to A and B in (b). They have the same value because of time reversal symmetry.

V. Interface transport

So far we have seen that the effect of chirality does not manifest itself in the topological classification or the existence of topological edge states, because unequal t_2 and t_3 just lead to the constant shift of the eigenvalues of the effective Hamiltonian. In this section, we discuss how chirality affects the interface transport by considering the dynamics of a classical harmonic-oscillator system with boundaries at which energy is injected [31]. One reason for using a classical system rather than a quantum one is that the meaning of the energy injection can be much more intuitively caught in a classical system as shown below (the energy injection is simply modeled by forced oscillation). Another reason is that the study of modulated honeycomb lattice model has been greatly developed in the context of classical systems like photonic crystals.

To calculate the interface transport, we denote dynamical variables by $\boldsymbol{x} = \{x_i\}$.

The equation of motion with respect to time τ is written as

$$\frac{d^2\boldsymbol{x}(\tau)}{d\tau^2} = -\Gamma\boldsymbol{x}(\tau) + \boldsymbol{f}^c \cos\Omega\tau. \tag{12}$$

Here Γ is a positive-definite dynamical matrix. An external force $\boldsymbol{f}^c \cos\Omega\tau$ is applied to the system with a frequency Ω, and the phase of the force is set to be the same at all sites. One can consider a variety of systems including spring-mass systems and LC-circuit systems, and the variables $\boldsymbol{x}$ and τ and the parameters are set dimensionless after rescaling of the length and time according to the specific system to be considered.

To facilitate the physical interpretation, let us solve Eq. (12) by using the normal mode decomposition [31]. By introducing an orthogonal matrix O that diagonalizes Γ, Eq. (12) becomes

$$\frac{d^2\tilde{\boldsymbol{x}}(\tau)}{d\tau^2} = -G\tilde{\boldsymbol{x}}(\tau) + \tilde{\boldsymbol{f}}^{(c)} \cos\Omega\tau, \tag{13}$$

where $G = O^T\Gamma O$, $\tilde{\boldsymbol{x}}(\tau) = O^T\boldsymbol{x}(\tau)$ and $\tilde{\boldsymbol{f}}^{(c)} = O^T\boldsymbol{f}^{(c)}$. The expression of Eq. (13) in component form becomes

$$\frac{d^2\tilde{x}_l(\tau)}{d\tau^2} = -\omega_l^2\tilde{x}_l(\tau) + \tilde{f}_l^{\,(c)} \cos\Omega\tau, \tag{14}$$

where we label the normal modes by an integer l. The solution of Eq. (14) for the initial condition $\boldsymbol{x}(\tau_{\rm init}) = d\boldsymbol{x}(\tau_{\rm init})/d\tau = 0$ is

$$\tilde{x}_l(\tau) = a_l^{(c)} \cos\Omega\tau + b_l^{(c)} \cos\omega_l\tau, \tag{15}$$

where

$$a_l^{(c)} = \frac{\tilde{f}_l^{\,(c)}}{\omega_l^2 - \Omega^2}, b_l^{(c)} = -a_l^{(c)}. \tag{16}$$

By reconstructing $\boldsymbol{x}(\tau)$ from these $\tilde{x}_l(\tau)$, one can understand the dynamics of the system.

Now, let us return to the interface transport, and consider a specific system illustrated in FIG. 6. We consider a ribbon structure of 10 hexagonal unit cells with $t_1 = 1.2$ cladded from both sides by 5 hexagonal unit cells with $t_1 = 0.8$. We also set $t_2 = -t_3 = 0.3$ in all region. To analyze the dynamics, we construct the dynamical

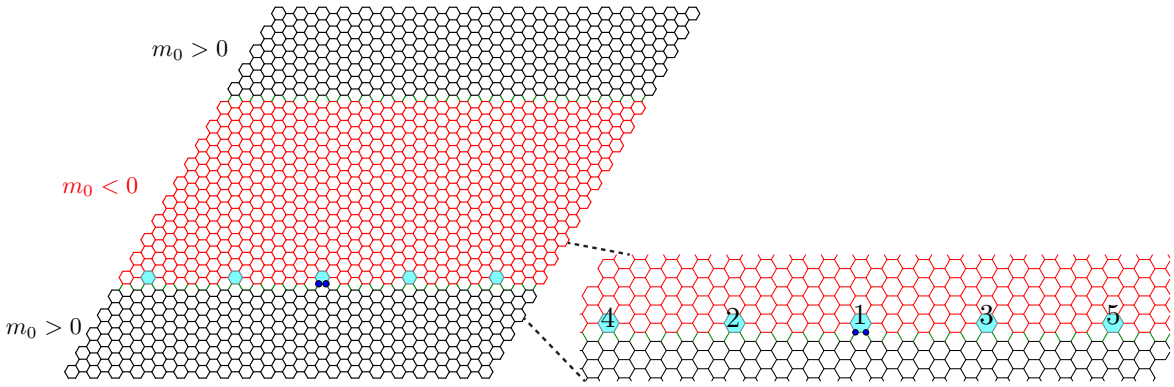

FIG. 6. (color online) Schematic illustration of the system consisting of regions with different topology. we set $t_2 = -t_3 = 0.3$ in all region. For the mass term part, we set $m_0 = -0.2$ for the $m_0 < 0$ region and $m_0 = 0.2$ for the $m_0 > 0$ region. 20 unit cells are lined up in the $\boldsymbol{a}_1$ and $\boldsymbol{a}_2$ directions with periodic boundary condition. We apply the external force $\boldsymbol{f}^{(c)}$ at the points of the boundary indicated by blue dots with the amplitude $f_0 = 1$.

matrix of this ribbon structure by the procedure Eq. (4), and calculate time evolutions of the intensity at each site i defined as

$$I_i = \frac{1}{2}\Big[\Omega^2 x_i^2 + \left(\frac{dx_i}{d\tau}\right)^2\Big], \tag{17}$$

using Eq. (12). Equation (17) is designed to eliminate the fast oscillation and focus on effective propagation of energy in a long time scale. We also choose $\epsilon = 3.1$ and $\Omega = \sqrt{\epsilon}$. This choice makes Γ positive definite, and Ω is in the bulk gap of the dynamical matrix Γ.

The obtained results are shown in FIG. 7. In FIG. 7(a), the lines labeled by 1-5 correspond to the intensities in the unit cells 1-5 defined in FIG. 6. The energy is injected at the unit cell 1, and the unit cells 2 and 3 (and also 4 and 5) are located at equal distances from the unit cell 1. The obtained difference between the intensities at 2 and 3 (4 and 5) reveals an asymmetric energy propagation caused by the effect of chirality. This novel asymmetry is prohibited in the achiral case $t_2 = t_3 = 0$. It should be noted that t_2 and t_3 are parameters that control the asymmetry. If the values of t_2 and t_3 are interchanged, an asymmetric energy propagation in the opposite direction

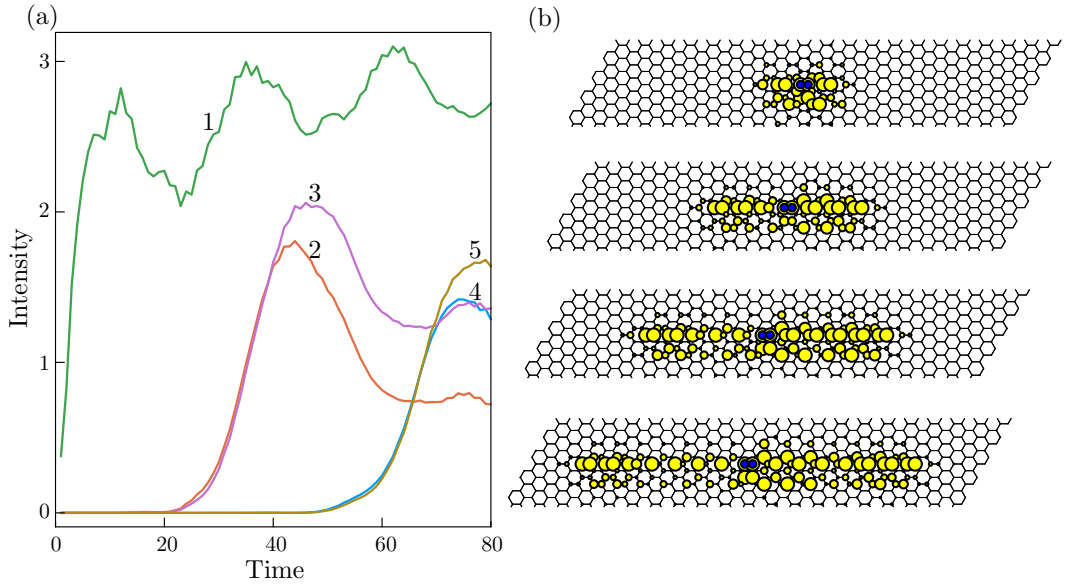

FIG. 7. (color online) (a) Time evolution of Intensity. The labels 1 to 5 correspond to those in FIG.6. Intensity in this figure is the sum over the six sites in the blue shaded hexagon in FIG.6. (b) Real space plot of the propagation of Intensity I_i. We show snapshots at $t = 15, 30, 45, 60$. An asymmetric propagation is achieved due to chirality.

is observed. In addition, as can be seen from Eqs. (15) and (16), the contribution of the modes with ω_l close to the frequency Ω dominates the energy propagation. The chirality effects of t_2 and t_3 manifest themselves in $\boldsymbol{x}(\tau)$ and intensity I_i as a linear combination of these multiple modes.

In the achiral case found in the literature, to select right-moving or left-moving interface states, the phase shifts are required in input terminals [32]. In our case, no phase shift is assumed in the forced oscillation term, which gives another way to control energy propagation.

VI. Conclusion and discussion

We have proposed a universal tight-binding model for chiral two-dimensional systems. We have shown that the topological classification can be conducted by using the Dirac Hamiltonian, and confirmed the emergence of topological edge states. We have

also discovered a novel asymmetric edge current induced without any phase tuning at input terminals. These consideration could be a building blocks in exploring chiral topological materials.

As noted in Sec.V, experimental realization of the system proposed in the present study would be more promising in classical systems because the fabrication of the system and the tuning of the interactions will be easier than for quantum systems. Photonic crystal of a dielectric material [25, 33] could be one direction, and top-down fabrication techniques now enable the realization of topological photonics in the visible wavelength regime [34]. Careful fabrication of chiral structures would provide an ideal platform for the experimental verification of the asymmetric transport discussed in Sec. 5. Self-organization of chiral soft materials could also be used for the preparation of systems that allows the investigation of chiral transport phenomena, and their ideal conditions could be achieved by the tunability of the structural properties of the soft material by external stimuli. Recently self-assembly of bowtie-shaped nanoparticles has been shown to exhibit tunable chiral photonic properties [35]. Chiral liquid crystals [36] can also offer a platform for self-organized tunable chiral structures, and a hexagonal lattice of skyrmions exhibited by a chiral liquid crystal [37] could host asymmetric transport phenomena in the visible wavelength regime. Classical mechanics of course provides a clue to the realization of systems for chiral topological transport phenomena, such as mass-spring systems discussed in Sec.V [29], and spinning top systems [38]. We hope that the present study will stimulate experimental studies towards the realization and observation of asymmetric topological transport phenomena in a system with time-reversal symmetry.

Acknowledgements

G. Y. is supported by the Kyushu University Leading Human Resources Development Fellowship Program. This study is also supported by JSPS KAKENHI No. JP21H01049 (J. F.) and No. JP20K03844 (T. K.).

Appendix A: Derivation of the effective Hamiltonian

To derive the effective Hamiltonian, we focus on the eigenstates at the Γ point, i.e. $\boldsymbol{k}_\Gamma = \boldsymbol{0}$. The following derivation is in parallel with the supplementary materials of the previous study [39], but any terms with t_2 and t_3 are new. The eigenstates of $H(\boldsymbol{k} = \boldsymbol{k}_\Gamma)$ are given by

$$\begin{aligned}
|f_{y(3x^2-y^2)}\rangle &= (-1,-1,-1,1,1,1)^T/\sqrt{6}, \\
|p_x\rangle &= (0,-1,1,0,1,-1)^T/2, \\
|p_y\rangle &= (2,-1,-1,-2,1,1)^T/2\sqrt{3}, \\
|d_{x^2-y^2}\rangle &= (-2,1,1,-2,1,1)^T/2\sqrt{3}, \\
|d_{xy}\rangle &= (0,1,-1,0,1,-1)^T/2, \\
|s\rangle &= (1,1,1,1,1,1)^T/\sqrt{6}.
\end{aligned} \tag{A1}$$

We use the conventional notation of s, p, d and f atomic orbitals. The corresponding eigenenergies are $E_{f_{y(3x^2-y^2)}} = -2t_0 - t_1 + 2t_2 + 2t_3$, $E_{p_x,p_y} = t_0 - t_1 - t_2 - t_3$, $E_{d_{x^2-y^2},d_{xy}} = t_1 - t_0 - t_2 - t_3$ and $E_s = 2t_0 + t_1 + 2t_2 + 2t_3$, respectively. In the following, we consider the case $E_{f_{y(3x^2-y^2)}} < E_{p_x,p_y,d_{x^2-y^2},d_{xy}} < E_s$. Based on these eigenstates, one can construct a low-energy effective Hamiltonian around the Γ point. Since we focus on the neighborhood of the Γ point where the bands are dominated by p and d states, it is sufficient to use $\{|p_x\rangle, |p_y\rangle, |d_{x^2-y^2}\rangle, |d_{xy}\rangle\}$ as the basis in calculating the effective Hamiltonian. By using these four eigenstates, we define the following pseudo-spin modes:

$$|p_\pm\rangle = \frac{1}{\sqrt{2}}(|p_x\rangle \pm i\,|p_y\rangle), \tag{A2}$$

$$|d_\pm\rangle = \frac{1}{\sqrt{2}}(|d_{x^2-y^2}\rangle \pm i\,|d_{xy}\rangle). \tag{A3}$$

In order to consider the effective Hamiltonian, it is convenient to introduce the following basis:

$$|u_\pm\rangle = \frac{1}{\sqrt{2}}(\mp i\,|p_\pm\rangle - |d_\mp\rangle), \tag{A4}$$

$$|l_\pm\rangle = \frac{1}{\sqrt{2}}(i\,|p_\pm\rangle \mp |d_\mp\rangle). \tag{A5}$$

Here, the explicit expression of $\{|u_-\rangle, |u_+\rangle, |l_-\rangle, |l_+\rangle\}$ is

$$|u_\pm\rangle = \begin{pmatrix} |\pm\rangle \\ 0 \end{pmatrix}, |l_\pm\rangle = \begin{pmatrix} 0 \\ \pm|\pm\rangle \end{pmatrix}, \tag{A6}$$

where

$$|\pm\rangle = \begin{pmatrix} 1 \\ \omega_\pm \\ \omega_\mp \end{pmatrix}, \omega_\pm = -\frac{1}{2} \pm \frac{\sqrt{3}}{2} i. \tag{A7}$$

Now, let us first calculate the low-energy effective Hamiltonian by using $\{|u_-\rangle, |u_+\rangle, |l_-\rangle, |l_+\rangle\}$. Indeed, if we expand the Hamiltonian in the basis, the effective Hamiltonian becomes

$$\mathcal{H}^{(\text{eff})}(k_x, k_y) = \begin{pmatrix} \langle -| F |-\rangle & \langle -| F |+\rangle & -\langle -| D |-\rangle & \langle -| D |+\rangle \\ \langle +| F |-\rangle & \langle +| F |+\rangle & -\langle +| D |-\rangle & \langle +| D |+\rangle \\ -\langle -| D^\dagger |-\rangle & -\langle -| D^\dagger |+\rangle & \langle -| F^T |-\rangle & \langle -| F^T |+\rangle \\ \langle +| D^\dagger |-\rangle & \langle +| D^\dagger |+\rangle & \langle +| F^T |-\rangle & \langle +| F^T |+\rangle \end{pmatrix}. \tag{A8}$$

Then, we perform the Taylor expansion up to the first order of the wavevectors. The effective Hamiltonian is approximated as

$$\mathcal{H}^{(\text{eff})}(k_x, k_y) \simeq -(t_2 + t_3) I \otimes I + (t_0 - t_1)\sigma_x \otimes \sigma_z + \frac{t_1 |\boldsymbol{a}_1|}{2} \sigma_x \otimes (\boldsymbol{k} \cdot \boldsymbol{\sigma}), \tag{A9}$$

where I is the identity matrix and $\sigma_i (i = x, y, z)$ is the Pauli matrices. We denote the Kronecker product as $\otimes$. It is shown that Eq.(A9) can be written as the Dirac Hamiltonian by introducing the following new basis:

$$|1\rangle = i\,|p_-\rangle = \frac{|u_-\rangle + |l_-\rangle}{\sqrt{2}}, \tag{A10}$$

$$|2\rangle = -\,|d_-\rangle = \frac{|u_+\rangle + |l_+\rangle}{\sqrt{2}}, \tag{A11}$$

$$|3\rangle = -i\,|p_+\rangle = \frac{|u_+\rangle - |l_+\rangle}{\sqrt{2}}, \tag{A12}$$

$$|4\rangle = -\,|d_+\rangle = \frac{|u_-\rangle - |l_-\rangle}{\sqrt{2}}. \tag{A13}$$

Using these new bases, the effective Hamiltonian is rewritten as

$$\mathcal{H}^{(\mathrm{eff})}(k_x, k_y) \simeq \begin{pmatrix} H_+(k_x, k_y) & 0 \\ 0 & H_-(k_x, k_y) \end{pmatrix}, \tag{A14}$$

where

$$H_\pm(k_x, k_y) = -(t_2 + t_3)I + (t_0 - t_1)\sigma_z + \frac{t_1|\boldsymbol{a}_1|}{2}(\pm k_x\sigma_x + k_y\sigma_y). \tag{A15}$$

Thus, we obtain the Dirac Hamiltonian Eq.(A15) with the constant energy shift $-(t_2 + t_3)$.

Let us make a remark about the effect of t_2, t_3 from the point of topological classification. When $t_2 = t_3 = 0$, the original Hamiltonian proposed by Wu and Hu [24] is retrieved. The effective Hamiltonian Eq.(A15) becomes

$$H_\pm(k_x, k_y) = (t_0 - t_1)\sigma_z + \frac{t_1|\boldsymbol{a}_1|}{2}(\pm k_x\sigma_x + k_y\sigma_y). \tag{A16}$$

Therefore, topological classification by using mass term $m := t_0 - t_1$ survive in this case. Moreover, the matrix F in Eq.(5) becomes the zero matrix, and the Hamiltonian has the sublattice symmetry

$$\gamma H(\boldsymbol{k})\gamma^\dagger = -H(\boldsymbol{k}), \gamma^2 = 1 \tag{A17}$$

with

$$\gamma = \begin{pmatrix} 1 & 0 & 0 & 0 & 0 & 0 \\ 0 & 1 & 0 & 0 & 0 & 0 \\ 0 & 0 & 1 & 0 & 0 & 0 \\ 0 & 0 & 0 & -1 & 0 & 0 \\ 0 & 0 & 0 & 0 & -1 & 0 \\ 0 & 0 & 0 & 0 & 0 & -1 \end{pmatrix}. \tag{A18}$$

In this case, thanks to this sublattice symmetry, one can define mirror winding number [40], and topological classification can be conducted mathematically rigorously. In the case $t_2 \neq 0$ and $t_3 \neq 0$, however, the sublattice symmetry is broken, and one can not choose the strategy to use the mirror winding number in classifing topological phase.

Appendix B: Berry bands and $\mathbb{Z}_2$ phase

Here, we basically follow the arguments in Ref. [30] to explain the idea of the Berry bands. We reproduce the arguments here since the explicit form of the equations are important in our numerics.

1. Wilson loops

We consider a closed path $\mathcal{L}$ in momentum space, and define the Wilson loop operator for $\mathcal{L}$ as

$$\hat{W}_{\mathcal{L}}^{\{n\}}(\boldsymbol{k_1}) := \hat{P}(\boldsymbol{k}_1)\hat{P}(\boldsymbol{k}_N)\cdots\hat{P}(\boldsymbol{k}_2)\hat{P}(\boldsymbol{k}_1), \tag{B1}$$

where $\hat{P}(\boldsymbol{k}_i)$ is a projection operator onto a chosen subspace$\{n\}$:

$$\hat{P}(\boldsymbol{k}_i) := \sum_{n\in\{n\}} |u_n(\boldsymbol{k}_i)\rangle \langle u_n(\boldsymbol{k}_i)| . \tag{B2}$$

Here, the sequence $\{\boldsymbol{k}_i\}_{i=1}^N$ represents closely spaced points along $\mathcal{L}$.

The eigenvalues and engenstates of the Wilson loop are obtained as follows. By using Bloch wave functions on the initial momentum $\boldsymbol{k}_1$, we can express it as a unitary matrix:

$$[W^{\{n\}}(\boldsymbol{k}_1)]_{ij} := \langle u_i(\boldsymbol{k}_1)|\, \hat{W}_{\mathcal{L}}^{\{n\}}(\boldsymbol{k_1})\, |u_j(\boldsymbol{k}_1)\rangle . \tag{B3}$$

The matrix $W^{\{n\}}(\boldsymbol{k}_1)$ can be diagonalized by a unitary matrix $V(\boldsymbol{k}_1)$, which satisfies

$$[V^\dagger(\boldsymbol{k}_1)W^{\{n\}}(\boldsymbol{k}_1)V(\boldsymbol{k}_1)]_{ij} = \delta_{ij}\exp(i\gamma_i), \tag{B4}$$

where γ_i is a gauge-invariant geometric phase, also known as a Berry phase. Therefore, the eigenstates of the Wilson loop are

$$|\tilde{u}_i(\boldsymbol{k}_1)\rangle = \sum_l [V(\boldsymbol{k}_1)]_{il}\, |u_l(\boldsymbol{k}_1)\rangle , \tag{B5}$$

with the corresponding eigenvalue being $\exp(i\gamma_i)$.

2. Berry bands

Let us now consider Wilson loops around an infinitesimally small path $\mathcal{L}'$ which enclose a point $\boldsymbol{k}$. Hereafter, to elucidate the topological nature of our system, we focus on the valence bands. First, we construct the Wilson loops as:

$$\hat{W}^{\rm val}_{\mathcal{L}'}(\boldsymbol{k}) := \hat{P}_{\rm val}(\boldsymbol{k}_1)\hat{P}_{\rm val}(\boldsymbol{k}_N)\cdots\hat{P}_{\rm val}(\boldsymbol{k}_2)\hat{P}_{\rm val}(\boldsymbol{k}_1). \tag{B6}$$

Here we denote $\{\boldsymbol{k}_i\}_{i=1}^N$s as closely spaced points along the path $\mathcal{L}'$, and $\hat{P}_{\rm val}(\boldsymbol{k}_i)$ is the projection operator onto the full valence band space.

Since the Wilson loop operator is unitary, we can define an associated Hermitian operator $\hat{H}_{\mathcal{F}}(\boldsymbol{k})$, given by

$$\hat{H}_{\mathcal{F}}(\boldsymbol{k}) := \lim_{A\to 0}\left[\frac{-i\log\hat{W}^{\rm val}_{\mathcal{L}'}(\boldsymbol{k})}{A}\right], \tag{B7}$$

where A is the area enclosed by $\mathcal{L}'$. The matrix form of this Hermitian operator is

$$\begin{aligned}[H_{\mathcal{F}}(\boldsymbol{k})]_{ij} &= \langle u_i(\boldsymbol{k})|\,\hat{H}_{\mathcal{F}}(\boldsymbol{k})\,|u_j(\boldsymbol{k})\rangle \\ &= \lim_{A\to 0}\left[\frac{-i[\log W^{\rm val}(\boldsymbol{k})]_{ij}}{A}\right],\end{aligned} \tag{B8}$$

where

$$[W^{\rm val}(\boldsymbol{k})]_{ij} := \langle u_i(\boldsymbol{k})|\,\hat{W}^{\rm val}_{\mathcal{L}'}(\boldsymbol{k})\,|u_j(\boldsymbol{k})\rangle\,. \tag{B9}$$

This matrix $H_{\mathcal{F}}(\boldsymbol{k})$ is Hermitian, and can be diagonalized by a unitary matrix $U(\boldsymbol{k})$ satisfying

$$[U^\dagger(\boldsymbol{k})H_{\mathcal{F}}(\boldsymbol{k})U(\boldsymbol{k})]_{ij} = \delta_{ij}\mathcal{F}_i(\boldsymbol{k}), \tag{B10}$$

where $\mathcal{F}_i(\boldsymbol{k})$ is the non-Abelian Berry curvature. Thus, the eigenvalue problem reads

$$\hat{H}_{\mathcal{F}}(\boldsymbol{k})\,|\tilde{u}'_i(\boldsymbol{k})\rangle = \mathcal{F}_i(\boldsymbol{k})\,|\tilde{u}'_i(\boldsymbol{k})\rangle\,, \tag{B11}$$

and

$$|\tilde{u}'_i(\boldsymbol{k})\rangle = \sum_l [U(\boldsymbol{k})]_{il}\,|u_l(\boldsymbol{k})\rangle\,. \tag{B12}$$

Following Ref. [30], we refer to these states as Berry bands.

3. $C_2\mathcal{T}$-protected $\mathbb{Z}_2$ phase

We first consider the spectrum of the Wilson loop built from projectors onto the three-dimensional valence bands in our model. We have calculated the Wilson loops along a sequence of parallel paths, $\mathcal{L}(t)$, as depicted in FIG. B.1, where these paths gradually traverse the Brillouin zone as t progresses from $t : 0 \to 1$.

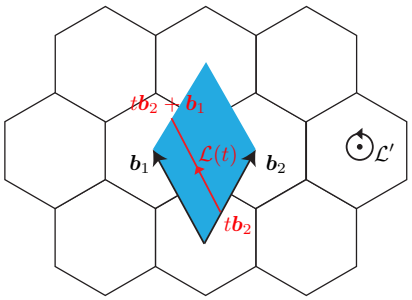

FIG. B.1. (color online) Schematic illustration of a path $\mathcal{L}(t)$ where Wilson loops are made on a series of these paths. These paths sweep the Brillouin zone (shaded blue region) as $t \to t+1$.

The Wilson loop spectra, as shown in FIG.B.2, indicate that the total windings of the Wilson loop spectra are zero. As mentioned in ref [30, 41], the total Chern number of the valence bands is equivalent to the total spectral winding of Wilson loops, and this result is consistent with the time-reversal symmetry.

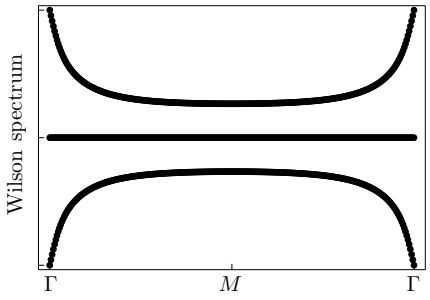

FIG. B.2. (color online) Wilson loop spectra for the topological region made through the valence bands. The total windings of these spectra are zero, as expected from time-reversal symmetry.

Alternatively, we can utilize the Berry bands introduced in the previous section. In $C_2\mathcal{T}$-symmetric crystals, the Hermitian operator $\hat{H}_{\mathcal{F}}(\boldsymbol{k})$ obeys the relation

$$(C_2\mathcal{T})\hat{H}_{\mathcal{F}}(\boldsymbol{k})(C_2\mathcal{T})^{-1} = -\hat{H}_{\mathcal{F}}(\boldsymbol{k}), \tag{B13}$$

which implies that each Berry curvature in a $C_2\mathcal{T}$-symmetric crystal is either zero or forms a positive/negative pair, as depicted in FIG.B.3. This constraint allows us the $\mathbb{Z}_2$ classification in $C_2\mathcal{T}$-symmetric systems.

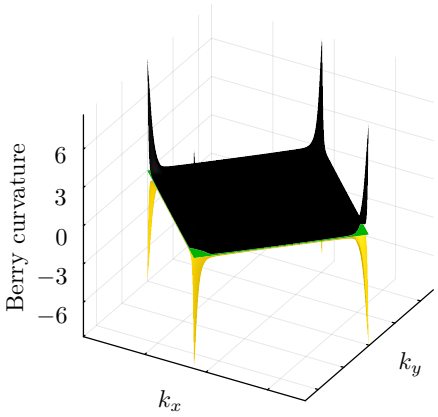

FIG. B.3. (color online) Berry curvature derived from the eigenvalue problem Eq.(B11). As a result of $C_2\mathcal{T}$ symmetry, these values are either zero or occur as positive/negative pairs.

Figure B.4 (a) shows the spectra of Wilson loops made separately through $\{|\tilde{u}'_i(\boldsymbol{k})\rangle\}_{i=1}^{3}$ for the same parameters as in FIG.B.2. There is no mixing, and the windings of the individual spectra are $\{w_{\text{negative}}, w_{\text{zero}}, w_{\text{positive}}\} = \{-1, 0, +1\} \mod 2$. On the other hand, for the trivial region, the windings are $\{w_{\text{negative}}, w_{\text{zero}}, w_{\text{positive}}\} = \{0, 0, 0\} \mod 2$, as indicated in FIG.B.4 (b).

[1] K. v. Klitzing, G. Dorda, and M. Pepper, New method for high-accuracy determination of the fine-structure constant based on quantized Hall resistance, Phys. Rev. Lett. **45**, 494 (1980).

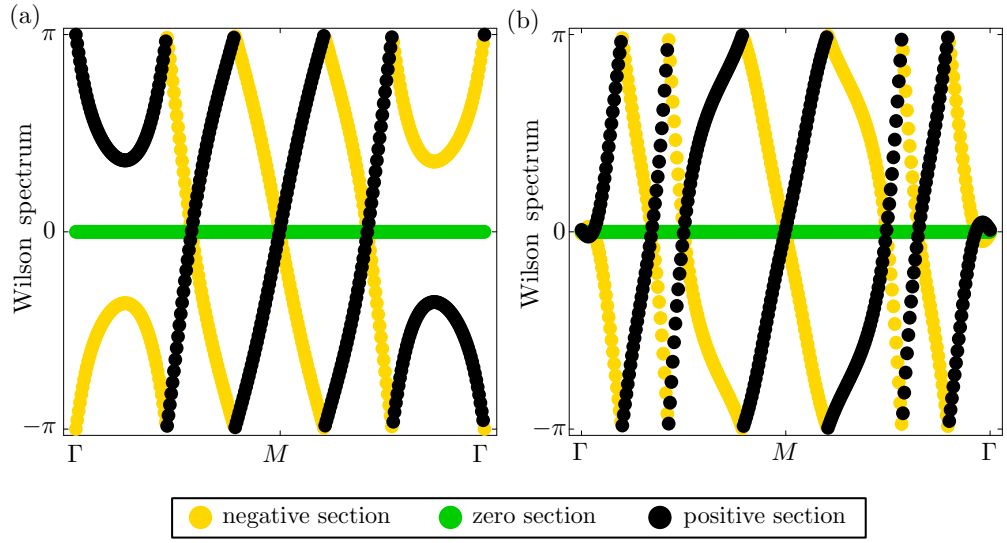

FIG. B.4. (color online) (a) Wilson loop spectra for the topological region made through the Berry bands. These spectra present well-defined nontrivial windings. The corresponding Z_2 index is shown to be protected by $C_2\mathcal{T}$ symmetry. (b) Wilson loop spectra for the topological region made through the Berry bands. These spectra present well-defined trivial windings, i.e. zero windings.

[2] D. J. Thouless, M. Kohmoto, M. P. Nightingale, and M. den Nijs, Quantized Hall conductance in a two-dimensional periodic potential, Phys. Rev. Lett. **49**, 405 (1982).

[3] C. L. Kane and E. J. Mele, Z_2 topological order and the quantum Spin hall effect, Phys. Rev. Lett. **95**, 146802 (2005).

[4] L. Fu and C. L. Kane, Topological insulators with inversion symmetry, Phys. Rev. B **76**, 045302 (2007).

[5] B. A. Bernevig, T. L. Hughes, and S.-C. Zhang, Quantum spin Hall effect and topological phase transition in HgTe quantum wells, Science **314**, 1757 (2006), https://www.science.org/doi/pdf/10.1126/science.1133734.

[6] L. Fu, Topological crystalline insulators, Phys. Rev. Lett. **106**, 106802 (2011).

[7] F. D. M. Haldane, Model for a quantum Hall effect without Landau levels: Condensed-matter realization of the "parity anomaly", Phys. Rev. Lett. **61**, 2015 (1988).

[8] M. Z. Hasan and C. L. Kane, Colloquium: Topological insulators, Rev. Mod. Phys. **82**, 3045 (2010).

[9] X.-L. Qi and S.-C. Zhang, Topological insulators and superconductors, Rev. Mod. Phys. **83**, 1057 (2011).

[10] C. L. Kane and E. J. Mele, Quantum spin Hall effect in graphene, Phys. Rev. Lett. **95**, 226801 (2005).

[11] F. Guinea, M. I. Katsnelson, and A. K. Geim, Energy gaps and a zero-field quantum Hall effect in graphene by strain engineering, Nature Physics **6**, 30 (2010).

[12] K. K. Gomes, W. Mar, W. Ko, F. Guinea, and H. C. Manoharan, Designer Dirac fermions and topological phases in molecular graphene, Nature **483**, 306 (2012).

[13] B. Hunt, J. D. Sanchez-Yamagishi, A. F. Young, M. Yankowitz, B. J. LeRoy, K. Watanabe, T. Taniguchi, P. Moon, M. Koshino, P. Jarillo-Herrero, and R. C. Ashoori, Massive Dirac fermions and Hofstadter butterfly in a van der Waals heterostructure., Science **340**, 1427 (2013).

[14] W. Yan, W.-Y. He, Z.-D. Chu, M. Liu, L. Meng, R.-F. Dou, Y. Zhang, Z. Liu, J.-C. Nie, and L. He, Strain and curvature induced evolution of electronic band structures in twisted graphene bilayer, Nature Communications **4**, 2159 (2013).

[15] Z. Qiao, S. A. Yang, W. Feng, W.-K. Tse, J. Ding, Y. Yao, J. Wang, and Q. Niu, Quantum anomalous Hall effect in graphene from Rashba and exchange effects, Phys. Rev. B **82**, 161414 (2010).

[16] G.-F. Zhang, Y. Li, and C. Wu, Honeycomb lattice with multiorbital structure: Topological and quantum anomalous Hall insulators with large gaps, Phys. Rev. B **90**, 075114 (2014).

[17] Q.-F. Liang, L.-H. Wu, and X. Hu, Electrically tunable topological state in [111] perovskite materials with an antiferromagnetic exchange field, New Journal of Physics **15**, 063031 (2013).

[18] M. Ezawa, Spin valleytronics in silicene: Quantum spin Hall–quantum anomalous Hall insulators and single-valley semimetals, Phys. Rev. B **87**, 155415 (2013).

[19] T. Oka and H. Aoki, Photovoltaic Hall effect in graphene, Phys. Rev. B **79**, 081406

(2009).

[20] T. Kitagawa, T. Oka, A. Brataas, L. Fu, and E. Demler, Transport properties of nonequilibrium systems under the application of light: Photoinduced quantum Hall insulators without Landau levels, Phys. Rev. B **84**, 235108 (2011).

[21] T. Uehlinger, G. Jotzu, M. Messer, D. Greif, W. Hofstetter, U. Bissbort, and T. Esslinger, Artificial graphene with tunable interactions, Phys. Rev. Lett. **111**, 185307 (2013).

[22] S. Raghu and F. D. M. Haldane, Analogs of quantum-Hall-effect edge states in photonic crystals, Phys. Rev. A **78**, 033834 (2008).

[23] Z. Wang, Y. D. Chong, J. D. Joannopoulos, and M. Soljačić, Reflection-free one-way edge modes in a gyromagnetic photonic crystal, Phys. Rev. Lett. **100**, 013905 (2008).

[24] L.-H. Wu and X. Hu, Topological properties of electrons in honeycomb lattice with detuned hopping energy, Scientific Reports **6**, 24347 (2016).

[25] L.-H. Wu and X. Hu, Scheme for achieving a topological photonic crystal by using dielectric material, Phys. Rev. Lett. **114**, 223901 (2015).

[26] N. Parappurath, F. Alpeggiani, L. Kuipers, and E. Verhagen, Direct observation of topological edge states in silicon photonic crystals: Spin, dispersion, and chiral routing, Science Advances **6**, eaaw4137 (2020), https://www.science.org/doi/pdf/10.1126/sciadv.aaw4137.

[27] A. Kitaev, V. Lebedev, and M. Feigel'man, Periodic table for topological insulators and superconductors, AIP Conference Proceedings (2009).

[28] S. Ryu, A. P. Schnyder, A. Furusaki, and A. W. W. Ludwig, Topological insulators and superconductors: tenfold way and dimensional hierarchy, **12** (2010).

[29] T. Kariyado and Y. Hatsugai, Manipulation of Dirac cones in mechanical graphene, Scientific Reports **5**, 18107 (2015).

[30] S. J. Palmer and V. Giannini, Berry bands and pseudo-spin of topological photonic phases, Phys. Rev. Res. **3**, L022013 (2021).

[31] T. Kariyado and R.-J. Slager, Selective branching and converting of topological modes, Phys. Rev. Res. **3**, L032035 (2021).

[32] Y. Li, Y. Sun, W. Zhu, Z. Guo, J. Jiang, T. Kariyado, H. Chen, and X. Hu, Topological

LC-circuits based on microstrips and observation of electromagnetic modes with orbital angular momentum, Nature Communications **9**, 4598 (2018).

[33] S. Barik, H. Miyake, W. DeGottardi, E. Waks, and M. Hafezi, Two-dimensionally confined topological edge states in photonic crystals, New Journal of Physics **18**, 113013 (2016).

[34] W. Liu, M. Hwang, Z. Ji, Y. Wang, G. Modi, and R. Agarwal, z_2 photonic topological insulators in the visible wavelength range for robust nanoscale photonics, Nano Letters **20**, 1329 (2020).

[35] P. Kumar, T. Vo, M. Cha, A. Visheratina, J.-Y. Kim, W. Xu, J. Schwartz, A. Simon, D. Katz, V. P. Nicu, E. Marino, W. J. Choi, M. Veksler, S. Chen, C. Murray, R. Hovden, S. Glotzer, and N. A. Kotov, Photonically active bowtie nanoassemblies with chirality continuum, Nature **615**, 418 (2023).

[36] H.-S.Kitzerow and C.Bahr, *Chirality in Liquid Crystals* (Springer, 2001).

[37] A. Nych, J.-i. Fukuda, U. Ognysta, S. Žumer, and I. Muševič, Spontaneous formation and dynamics of half-skyrmions in a chiral liquid-crystal film, Nature Physics **13**, 1215 (2017).

[38] L. M. Nash, D. Kleckner, A. Read, V. Vitelli, A. M. Turner, and W. T. M. Irvine, Topological mechanics of gyroscopic metamaterials, Proceedings of the National Academy of Sciences **112**, 14495 (2015).

[39] T. Kariyado and R.-J. Slager, π-fluxes, semimetals, and flat bands in artificial materials, Phys. Rev. Research **1**, 032027 (2019).

[40] T. Kariyado and X. Hu, Topological states characterized by mirror winding numbers in graphene with bond modulation, Scientific Reports **7**, 16515 (2017).

[41] M. Blanco de Paz, C. Devescovi, G. Giedke, J. J. Saenz, M. G. Vergniory, B. Bradlyn, D. Bercioux, and A. García-Etxarri, Tutorial: Computing topological invariants in 2D photonic crystals, Advanced Quantum Technologies **3**, 1900117 (2020), https://onlinelibrary.wiley.com/doi/pdf/10.1002/qute.201900117.